NOAA Technical Report ERL 316-AOML 16

U.S. DEPARTMENT OF COMMERCE
NATIONAL OCEANIC AND ATMOSPHERIC ADMINISTRATION
Environmental Research Laboratories

The Initial Water Circulation and Waves Induced by an Airflow

W. L. McLEISH
G. E. PUTLAND

BOULDER, COLO.
FEBRUARY 1975

ENVIRONMENTAL RESEARCH LABORATORIES

The mission of the Environmental Research Laboratories is to study the oceans, inland waters, the lower and upper atmosphere, the space environment, and the earth, in search of the understanding needed to provide more useful services in improving man's prospects for survival as influenced by the physical environment. Laboratories contributing to these studies are:

Atlantic Oceanographic and Meteorological Laboratories (AOML): Geology and geophysics of ocean basins and borders, oceanic processes, sea-air interactions and remote sensing of ocean processes and characteristics (Miami, Florida).

Pacific Marine Environmental Laboratory (PMEL): Environmental processes with emphasis on monitoring and predicting the effects of man's activities on estuarine, coastal, and near-shore marine processes (Seattle, Washington).

Great Lakes Environmental Research Laboratory (GLERL): Physical, chemical, and biological limnology, lake-air interactions, lake hydrology, lake level forecasting, and lake ice studies (Ann Arbor, Michigan).

Atmospheric Physics and Chemistry Laboratory (APCL): Processes of cloud and precipitation physics; chemical composition and nucleating substances in the lower atmosphere; and laboratory and field experiments toward developing feasible methods of weather modification.

Air Resources Laboratories (ARL): Diffusion, transport, and dissipation of atmospheric contaminants; development of methods for prediction and control of atmospheric pollution; geophysical monitoring for climatic change (Silver Spring, Maryland).

Geophysical Fluid Dynamics Laboratory (GFDL): Dynamics and physics of geophysical fluid systems; development of a theoretical basis, through mathematical modeling and computer simulation, for the behavior and properties of the atmosphere and the oceans (Princeton, New Jersey).

National Severe Storms Laboratory (NSSL): Torandoes, squall lines, thunderstorms, and other severe local convective phenomena directed toward improved methods of prediction and detection (Norman, Oklahoma).

Space Environment Laboratory (SEL): Solar-terrestrial physics, service and technique development in the areas of environmental monitoring and forecasting.

Aeronomy Laboratory (AL): Theoretical, laboratory, rocket, and satellite studies of the physical and chemical processes controlling the ionosphere and exosphere of the earth and other planets, and of the dynamics of their interactions with high-altitude meteorology.

Wave Propagation Laboratory (WPL): Development of new methods for remote sensing of the geophysical environment with special emphasis on optical, microwave and acoustic sensing systems.

Marine EcoSystem Analysis Program Office (MPO): Plans and directs interdisciplinary analyses of the physical, chemical, geological, and biological characteristics of selected coastal regions to assess the potential effects of ocean dumping, municipal and industrial waste discharges, oil pollution, or other activity which may have environmental impact.

Weather Modification Program Office (WMPO): Plans and directs ERL weather modification research activities in precipitation enhancement and severe storms mitigation and operates ERL's research aircraft.

NATIONAL OCEANIC AND ATMOSPHERIC ADMINISTRATION

BOULDER, COLORADO 80302

U.S. DEPARTMENT OF COMMERCE
Frederick B. Dent, Secretary

NATIONAL OCEANIC AND ATMOSPHERIC ADMINISTRATION
Robert M. White, Administrator
ENVIRONMENTAL RESEARCH LABORATORIES
Wilmot N. Hess, Director

NOAA TECHNICAL REPORT ERL 316-AOML 16

The Initial Water Circulation and Waves Induced by an Airflow

W. L. McLEISH
G. E. PUTLAND

BOULDER, COLO.
February 1975

For sale by the Superintendent of Documents, U. S. Government Printing Office, Washington, D. C. 20402

DISCLAIMER

The Environmental Research Laboratories do not approve, recommend, or endorse any proprietary product or proprietary material mentioned in this publication. No reference shall be made to the Environmental Research Laboratories, or to this publication furnished by the Environmental Research Laboratories, in any advertising or sales promotion which would indicate or imply that the Environmental Research Laboratories approve, recommend, or endorse any proprietary product or proprietary material mentioned herein, or which has as its purpose an intent to cause directly or indirectly the advertised product to be used or purchased because of this Environmental Research Laboratories publication.

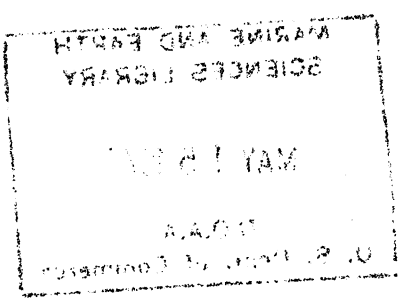

CONTENTS

THE INITIAL WATER CIRCULATION AND WAVES INDUCED BY AN AIRFLOW

W. L. McLeish and G. E. Putland

ABSTRACT

The early water circulation and waves under an airflow were examined in laboratory experiments. At a particular fetch or time, a waterflow undergoes a laminar-turbulent transition through an intermediate circulation pattern. Simultaneously the first, capillary-gravity waves undergo a correlated characteristic transition leading to separate capillary and gravity waves, and the wave energy increases markedly. Some of the energy of the current is transferred to the waves during the transition. A viscous sublayer lies at the surface above a turbulent flow, but is thinner than a corresponding sublayer at a solid boundary.

I. INTRODUCTION

The ocean surface is of major significance to sea-air interaction studies because many quantities enter and leave the ocean only through the surface. Unique mechanisms of transport dominate near it and often control the rates of transfers. Because of these mechanisms, properties of water near the surface are particularly sensitive to variations in exchange rates. As a result of these aspects of ocean processes, understanding and monitoring several air-sea interactions can be furthered through a study of the layer of water adjacent to the surface.

The present report examined the early patterns of water waves and flow in a wind-water tunnel. Mean water-velocity profiles very near the

surface were obtained with bubble tracers, deeper profiles in the main waterflow were measured with a submerged hot-film anemometer, and wave heights were recorded by a wave gage. Photographs showed the distinctive initial wave patterns, and an infrared radiation thermometer identified vertical mixing produced by water turbulence. The initial growths of wind-generated water current and waves were found to have interrelated characteristics not considered in present theories of sea-air interaction. In addition, a viscous sublayer adjacent to the surface above water turbulence was demonstrated, but found to be thinner than the corresponding sublayer at a solid boundary. The thinner water boundary layer implies less resistance to the transport of water properties to the surface than at a solid boundary.

II. EXPERIMENTAL METHODS

The basic construction of the wind-water tunnel was described by McLeish et al. (1971). A blower drew a smooth airflow over a 90- by 600-cm water surface. A plastic foam air filter was later installed, and a curved sheet of metal was used to damp waves at the downwind end of the tank. The water circulation appeared to approach equilibrium after a few minutes of operation. Some experiments examined effects of starting the airflow, either slowly by switching on the blower or rapidly by releasing the exhaust door while the blower was turning at full speed. The latter procedure caused noticeable water vibrations when the blocked blower was running and a seiche in the tank when the door slammed open. Some air leaked by the closed blower exhaust door.

The water was filtered to reduce scattered light in photographs and softened to prevent scale formation on the electrolysis wire in bubble photography experiments. In addition, hydrochloric acid was added to give a 0.04-percent concentration to increase the electrical conductivity of the water. While the air was flowing, the water surface was continuously cleaned by flowing over a barrier at the downwind end. The water level was maintained near the level of the entrance duct by continuous refilling during experiments. The room was kept dark between experiments to retard biological growth so that the water had to be changed only rarely. The water temperature was generally between the dry- and wet-bulb temperatures of the air.

Motions of water near the moving surface were measured by photographing clouds of microscopic hydrogen bubbles generated by electrolysis on a thin vertical wire through the surface. The quality of the bubble patterns was highly variable and depended largely on the condition of the wire surface and on the electrical pulses. Considerable efforts were required to develop adequate techniques for these measurements. A 0.001" gold alloy or platinum wire was soldered as a short extension to a copper wire support and inserted vertically into the water to a depth of a few millimeters. The lower end of the wire was free. The surface of the wire could be cleaned with aqua regia to give fair bubble patterns, but platinizing the wire surface or oscillating the wire with a vibrator was of no value. The performance of the wire surface could best be enhanced through electrolysis at a high rate. Application of -160 V to a wire submerged a short distance removed the

outer surface within a minute, and the remaining wire gave improved bubble patterns. One short section of wire was completely dissolved in 5 min of this treatment.

The electrical power supply unit provided negative 0 to 160 V d.c. pulses with an on-time fraction of 5 to 95 percent at 1/2 to 200 pulses per second and 200 mA current. An adjustable spike was produced at the beginning of each pulse. A negative 0 to 6 V bias was applied to the wire between pulses. Each pulse triggered a single photograph by a cine camera. A frequency counter recorded the pulse rate. The minimum overvoltage necessary for photography was used in the electrical pulses, and a negative bias barely generating bubbles was maintained between pulses. A pulse voltage of 2 to 5 V, with an on-time fraction of 20 to 50 percent and a fairly broad spike of 10 V, was often used. The resistance of the wire and water circuit during a pulse was on the order of 1,000 Ω. As many as 50 distinct bubble lines per second could be produced.

A 35-mm 16-fps cine camera viewed the bubble pattern crosswind at an upward angle of about 1/7 and with an image scale of 1:1. Light from a 5,000-W bulb on the opposite side of the tank was focused by a Fresnel lens and traveled slightly upwind and slightly upward through the water to the bubble area. The pulse that triggered each photograph was recorded with a six-channel light-beam oscillograph along with water height.

Figure 1 shows bubble-line patterns in a nearly laminar flow just upstream of the formation of steep waves. The merging of the lines downstream is attributed to cross-stream motion and not bubble rise

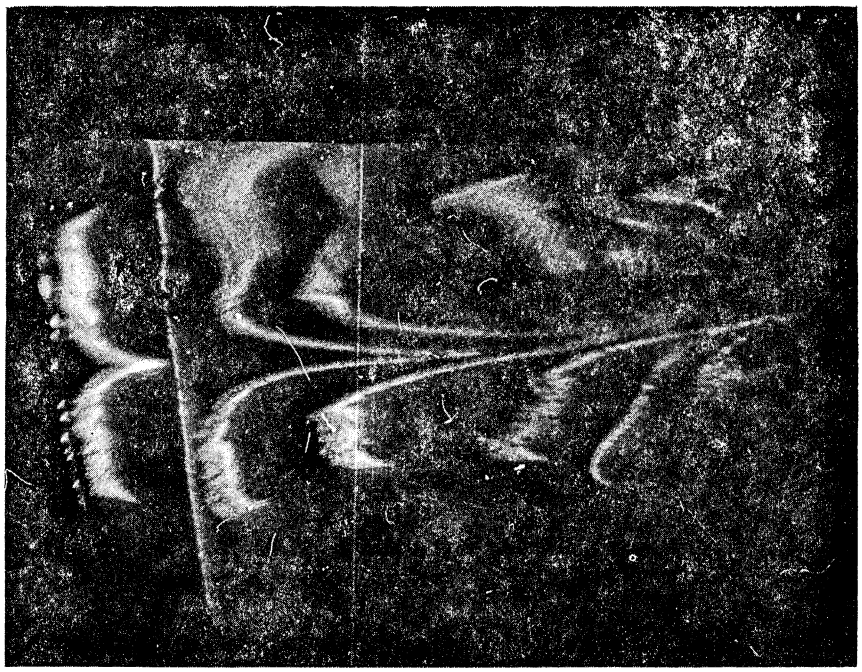

Figure 1. Bubble lines and surface reflections. The width of the photograph represents 24 mm in the direction of the flow. A curved line of bubbles is just leaving the electrolysis wire on the left, and the surface reflection gives a symmetry about a horizontal line. The vertical out-of-focus white line is the wire of a wave gage.

because the reflections are well separated, although ragged. However, only the newest two lines were used in the analysis. The bases of bubble lines appear to rise in this frame, but the mean motion was slightly downward.

The photograph of bubble lines in figure 2 was obtained in fully turbulent flow downstream. In general, the entire reflections and bubble lines were visible. However, because of irregularities of the reflections, only regions near the surface were used in the analysis.

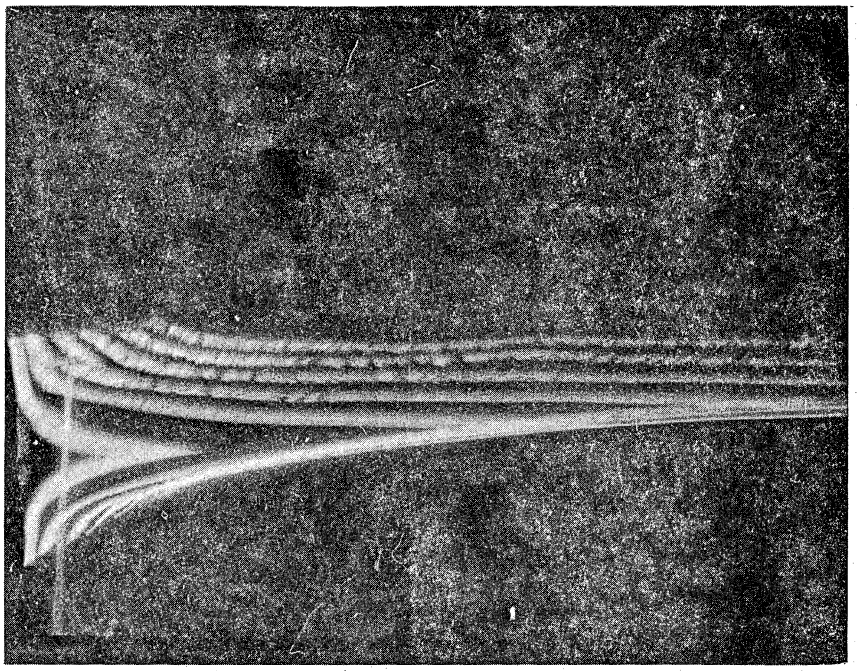

Figure 2. Bubble lines and surface reflections. The scene was rotated through the alinement of relay mirrors. The straightness of the image of a wave gage wire shows that the water surface was nearly level.

Hot-film anemometers recorded velocities in the air and in the water. These data are Eulerian in nature, in contrast with the bubble-tracer measurements which are Lagrangian and include wave currents.

Water heights were recorded with a wave gage similar to one described by Hires (1968). The frequency response of this instrument was not tested directly; however, its performance beneath wind waves was compared with that of a submerged hot-film anemometer. In one experiment, the wave gage recorded 17 wave crests/sec while the anemometer recorded 19 velocity maxima/sec. In another experiment, 17 wave crests/sec were measured with 21 velocity maxima/sec. Because the

anemometer response was biased toward high frequency waves, it appears that the wave gage was capable of recording water waves near these frequencies.

In addition, a true rms voltmeter and an infrared radiation thermometer were used in some experiments, and compacted surface films, floating dust, and dye streaks were studied in others. Photographic and visual observations of the initial waveforms were best made with the room darkened, the water surface illuminated from within the air entrance duct, and the waveforms viewed from the downwind end of the tank near the water surface.

III. DATA ANALYSIS

Enlarged projections of the first two free-drifting bubble lines and their surface reflections (see figs. 1 and 2) were traced onto paper, and the tracings were digitized. The data were analyzed by a computer through rotation of axes, determination of the depth of each reading by interpolation between the direct and reflected images, a second interpolation to fixed depths, subtraction between the two bubble lines, and averaging a number of frames. In addition, the apparent height of the midpoint between a point on a bubble line and its reflection was used to calculate a mean crosswind velocity V where the waves were not steep. The mean difference in depths of the bases of the two bubble lines in a single frame was also calculated. Errors in the calculation caused by slopes of the water surface were reduced by

averaging several measurements. Unreadable frames were omitted; and the experiment was discarded if there were several unreadable frames.

It is difficult to estimate the accuracy of the bubble measurements. The equipment was designed to measure positions to 0.01 cm, but greater errors could have arisen in interpreting the photographs. Buoyant rise of the bubbles would lead to further errors, but the rise rate calculated for 25-μ diameter bubbles--according to the modified Stokes equation $W = g\rho a^2/3\mu$--gave a vertical rise between frames of only 0.004 cm. Interference to the flow by the wire decreases the water velocity, but the results of Schraub et al. (1964) indicated this error in the present measurements to be negligible. Acceleration, or spinup, of the water circulation may not have progressed to an equilibrium in these experiments, and the velocity profiles represent relative, not absolute, velocities.

One experiment (fig. 6 below) was performed among steep waves that gave significant rotations to the bubble-line patterns. Mean water velocities were calculated first by rotating the axes so that the surface intersections of the two bubble lines appeared at the same height and again by rotating so that the average of the two bubble-line-plus-reflection images was upright. The mean absolute difference in rotation was 9°, but the mean surface velocities differed by only 3 percent.

Chart records containing other measurements were digitized and the data averaged. Wave records often had smooth envelopes which could be analyzed separately. The envelope widths, calculated as wave energy,

were compared with measurements from the true rms voltmeter. The data from wave envelopes showed faster and greater rises and falls in wave energy than did the voltmeter. In addition, the wave envelopes were so traced as not to include any seiche or other low frequency waves present in the tank.

Photographs of the upwind water surface show that the initial steep waves occurred as short-crested dimples moving downstream in somewhat irregular rows. A wave or water current recording at one point might or might not be in a wave row at a particular time. Because a wave row remained in one position for a few seconds, averages were extended in experiments within the rows.

Wave energy was calculated in erg/cm^2 according to

$$E_{total} = 2 \cdot E_{potential} = \rho g \overline{\eta^2}$$

where η^2 is the variance of water height fluctuations. This equation is accurate only for gravity waves; however, the energy of capillary waves is small generally in comparison with that of gravity waves.

IV. OBSERVATIONS

Figures 3 through 6 show mean water-velocity profiles near the surface obtained from bubble photographs. Figure 3 was derived from a series including figure 1, and figure 6 was derived from a series including figure 2. The accompanying table 1 gives the experimental conditions. Empirically fitted exponential curves $U = a e^{-bz}$ were drawn in figures 3 through 5 to illustrate the smoothness of the data. The

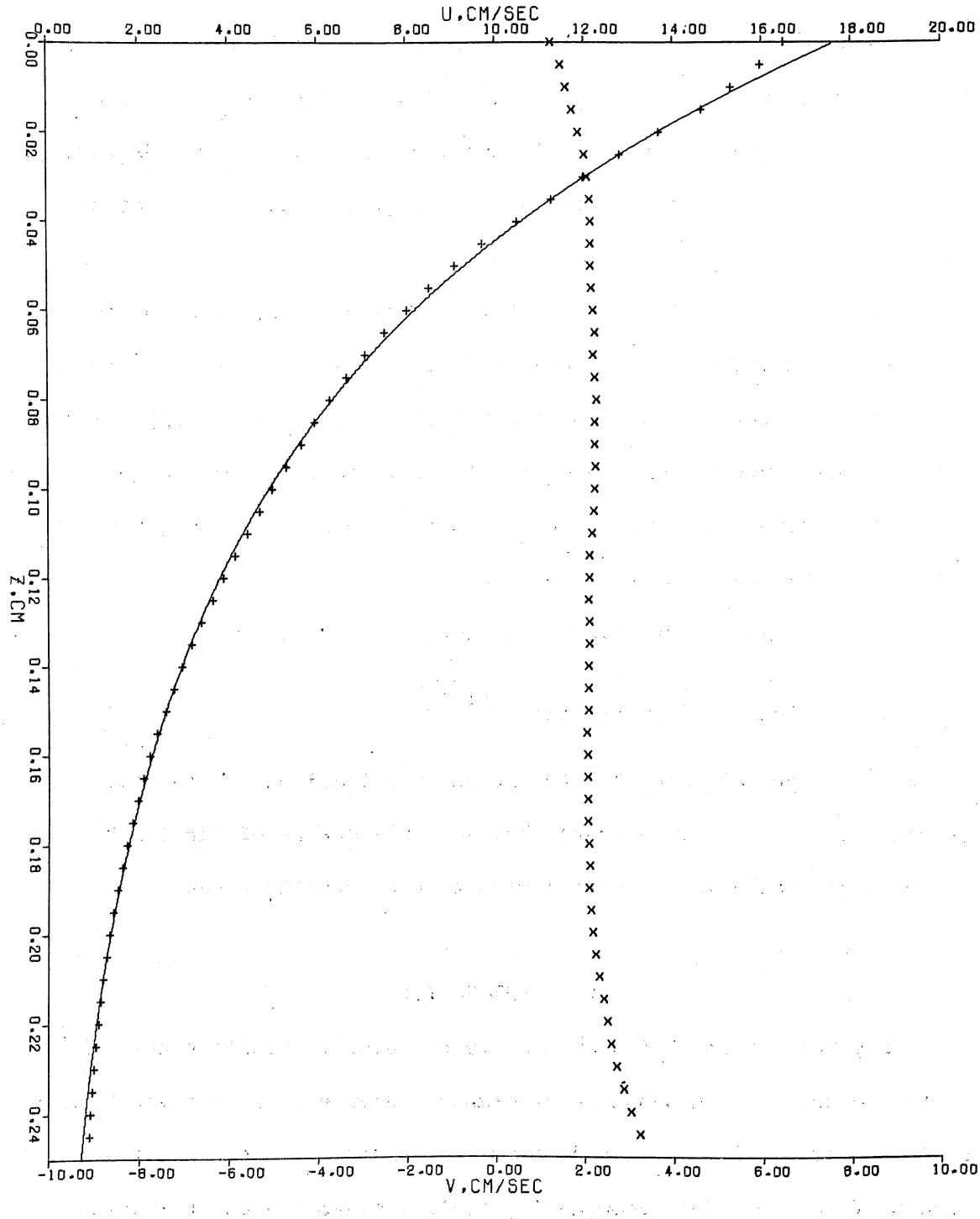

Figure 3. Mean water-velocity profile. Downstream (+) and cross-stream (x) velocity components were derived from bubble lines. The solid line is the rms best-fit exponential curve to the downstream data.

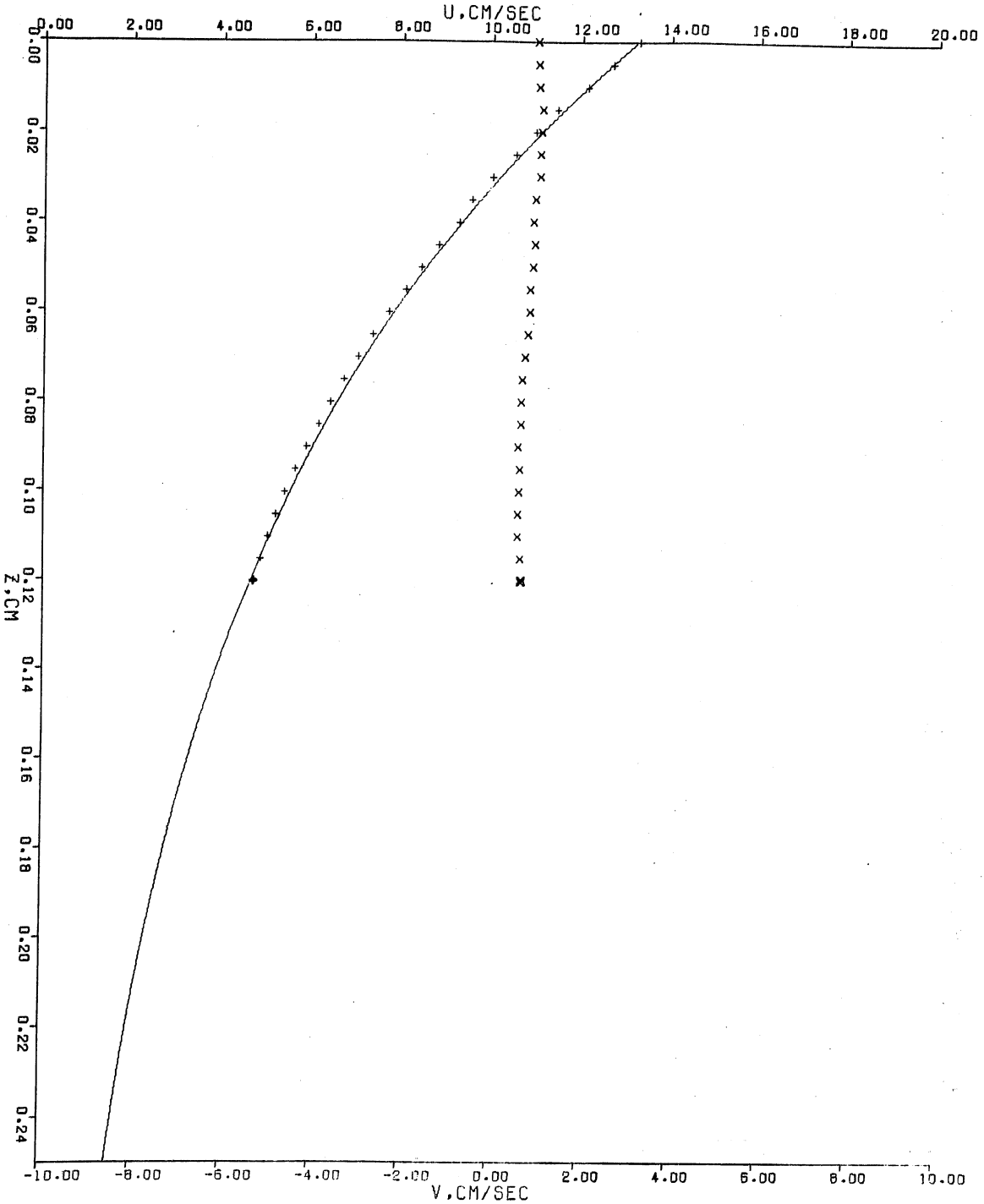

Figure 4.. Mean water-velocity profile. Downstream (+) and cross-stream (x) velocity components were derived from bubble lines. The solid line is the rms best-fit exponential curve to the downstream data.

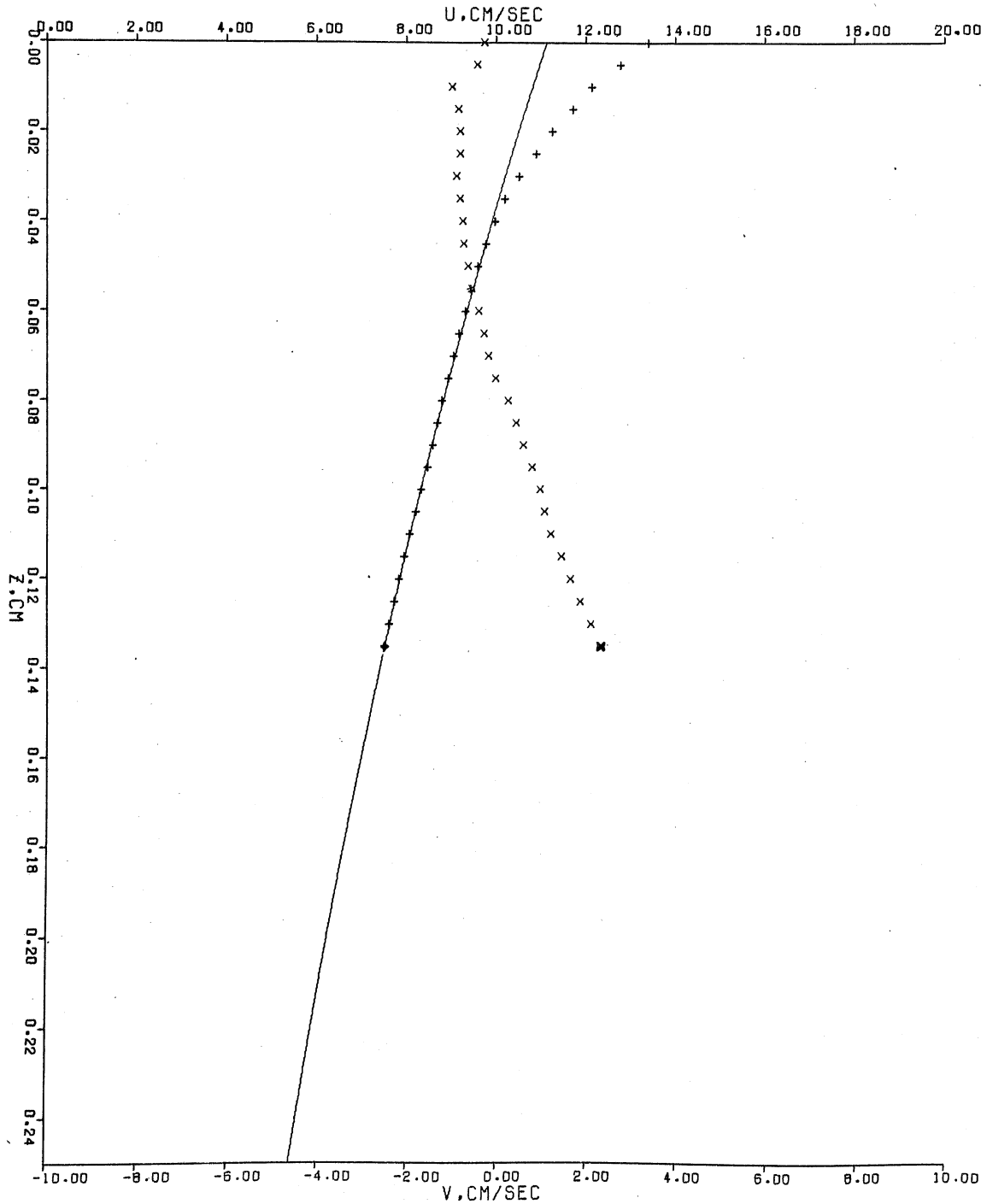

Figure 5. Mean water-velocity profile. Downstream (+) and cross-stream (x) velocity components were derived from bubble lines. The solid line is an exponential curve fitting the deeper downstream data.

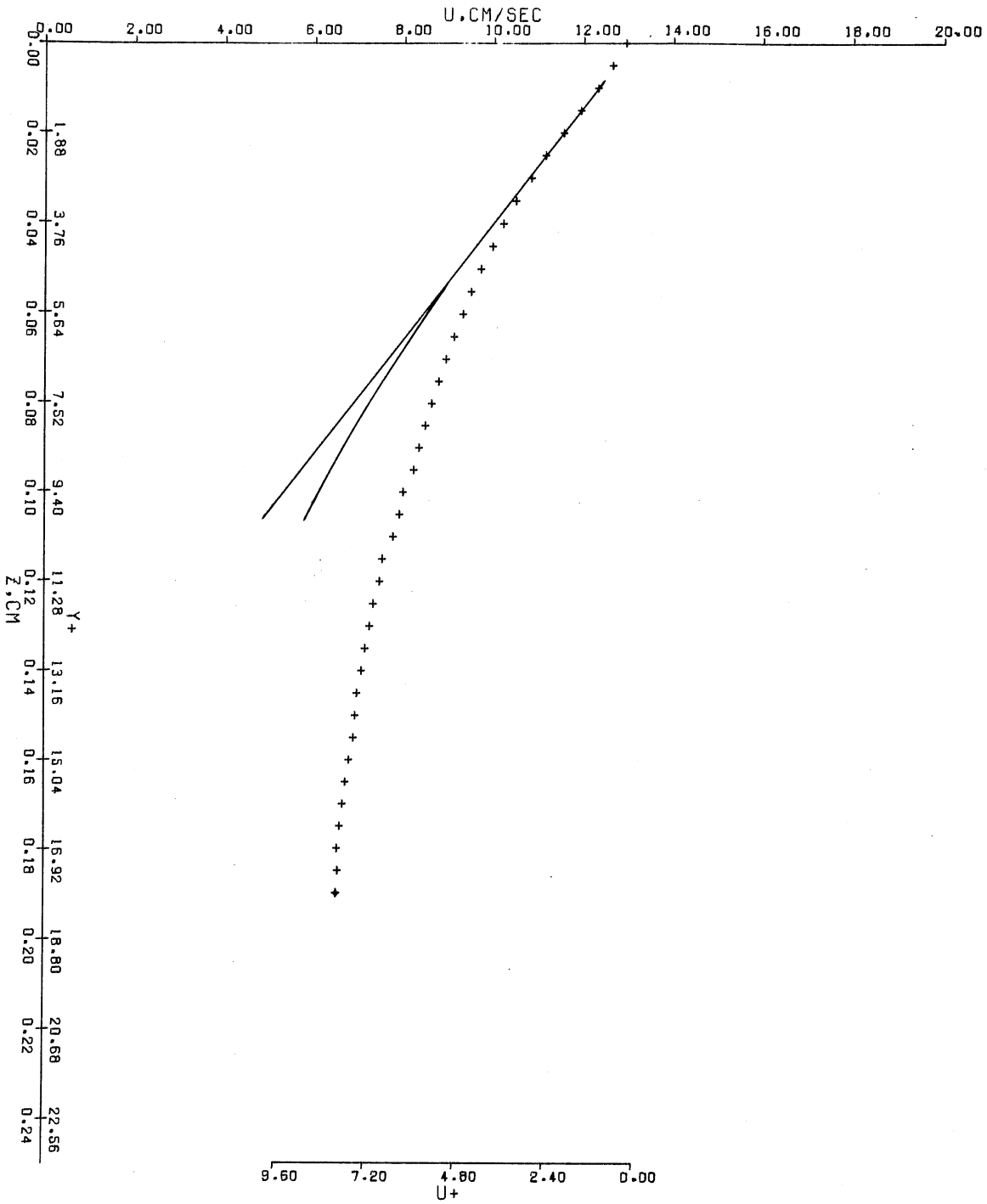

Figure 6. Downstream component of mean water-velocity profile. The straight line is fitted to the slope near the surface, and the curved departure represents the profile at a solid boundary in dimensionless units Y+ and U+.

Table 1. Water Velocity Measurements from Bubble Photographs

Figure	3	4	5	6
Number of frames analyzed	46	11	17	37
Duration of experiment, sec	3.5	10	26	4.3
U_a, cm/sec	900	550	600	550
Fetch, cm	24	25	69	382
Location	early wave rows	above wave rows	within wave rows	below wave rows
Best exponential fit				
a, cm/sec	18.3	13.6	—	—
b, cm^{-1}	12.4	8.6	—	—
rms ϵ, cm/sec	0.15	0.15	—	—
$\bar{W}$, cm	-0.017	-0.002	+0.005	-0.056
Stress, dynes/cm^2	2.0	1.0	1.2	0.7

curve in figure 5 approximates only a portion of the profile. The best exponential fit and the rms departure of the mean velocity values from the fit were obtained with a computer. The mean depth difference between the bases of successive bubble lines is given in the table as $\overline{W}$ where a positive value represents a mean rise. The surface stress τ_0 was calculated from the exponential curves in figures 3 and 4 and from the smoothed surface velocity gradient in figures 5 and 6. The longer durations in figures 4 and 5 resulted from analyzing only 1 frame/sec. Another analysis of the run in figure 6, not presented, extended over 85 sec but gave a profile similar to that shown in the figure.

The bubble-line photographs allow measurements of water velocity very near the surface, even among waves of some steepness, although the accuracies in figures 5 and 6 were decreased by wave shapes. The mean velocity profiles in figure 3 were obtained in the early laminar-turbulent zone where the flow was largely laminar in nature. The downstream velocity component U fit a smooth curve well. The cross-stream component V also fit a smooth curve, although it was offset. Both profiles showed departures near the surface, attributed to airflow interference by equipment mounted asymmetrically above the bubble wire. The buoyancy-induced vertical motion between frames was small.

The velocities in figure 3 fluctuated rapidly between frames. The rms fluctuation at a depth was about 15 percent of the mean velocity at that depth. The depth-averaged variance, reduced by the number of frames in the average, led to a calculated rms fluctuation of the average of 0.16 cm/sec, comparable to the observed rms departure of the mean

profile from the fitted smooth curve. The correlation of fluctuations at depth with the surface fluctuations showed a rapid decrease with depth, reaching a value of 0.5 at a depth of 0.035 cm, then remaining near 0.3 to 0.4 at greater depths. Because the theoretical correlation caused by sinusoidal water waves is unity at all depths, the shape of the correlation curve indicates very shallow, rapid fluctuations possibly caused by fluctuations in air stress. The kurtosis of the frequency distribution of surface fluctuations was -0.2, compared with 0 for a normal distribution and with -1.2 for a uniform distribution. This value is in accord with the possibility that the surface fluctuations were largely turbulent in origin.

A mean surface stress of 2.0 dynes/cm^2 was indicated by the surface shear in figure 3. It appears that the stress was not constant with fetch, but was disturbed by an irregularity at the upwind edge of the water. This is supported by observations of changes in the fetch at which the waveforms underwent transition when the water level was changed slightly.

The data in figure 4 were obtained at a lower airspeed well before transition so that the flow was solely a developing laminar boundary layer. The profile fit a smooth curve well, with a calculated stress of 1.0 dynes/cm^2. Figure 5 was obtained within the laminar-turbulent transition shown by the wave patterns and is of an intermediate shape not fitting a simple analytic curve. The indicated stress is close to that in figure 4.

Figure 6 was obtained well downstream where both the circulation and the waves represented the little-changing pattern of development beyond the early transition. A straight line representing the surface shear is included, and a curve is drawn to show the departure from a linear profile observed in a turbulent transition layer at a solid boundary. This curve was calculated using the observed surface stress and average measurements from graphs of turbulent boundary-flow profiles given by Mellor and Herring (1969) and by Kline et al. (1967) in non-dimensional form. The viscous sublayer at the free surface is roughly one-half as thick as at a solid boundary. The different thickness may indicate that the value of von Karman's constant k is larger in turbulence at a free boundary. Also, the indicated surface stress supported by water shear is less than upstream, although other measurements indicate the total stress to be greater. The decrease might be attributed to the effects of waves on momentum transport.

Figure 7 shows mean water velocity measured by a hot-film anemometer at different depths as a function of fetch with a midstream airspeed of 850 cm/sec. Mean water velocities obtained from a submerged hot-film anemometer extend to greater depths than do the bubble-line photographs, although such data are not available near a wavy surface. The "zero" depth readings here were obtained at the minimum continuously submerged depth of the probe. The dip in the "zero" depth plot was found in two additional series of measurements. The water velocities in figure 7 show an initial rise in surface water velocity

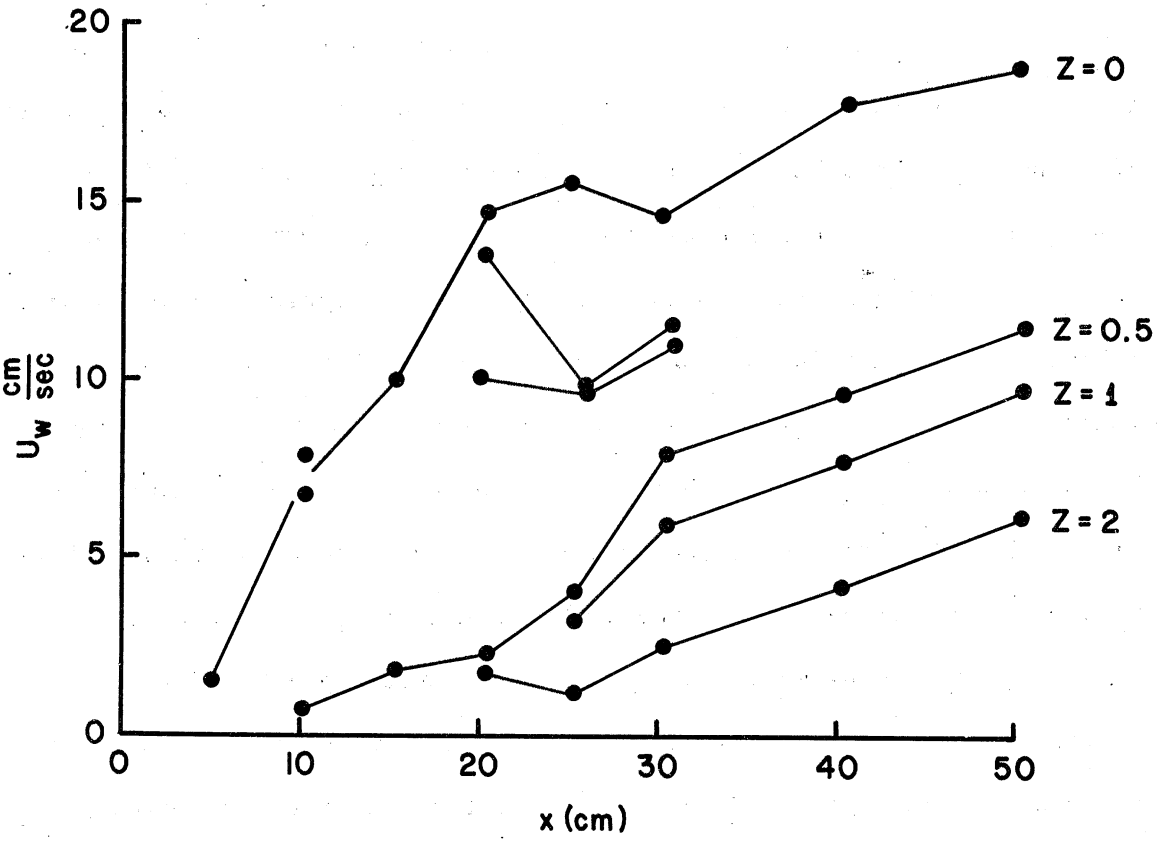

Figure 7. Mean water velocity versus fetch at different depths.

and deeper increases farther downstream, as expected for a developing laminar boundary layer. A dip in surface velocity and a rapid acceleration below mark the beginning of vertical mixing by turbulence and occur at the rapid growth of waves.

Another set of these measurements is contoured in figure 8 as a vertical longitudinal section of water velocity. A laminar boundary layer developed to a depth of 0.5 cm in the first 20 cm of fetch. Then the near-surface velocity decreased between 25 and 35 cm of fetch while the flow below accelerated rapidly. Farther downstream, the mean velocities increased again as a turbulent boundary layer. The onset of vertical mixing is most clearly demonstrated in the velocity difference between the surface and a depth of 0.5 cm. The mean difference was 11 cm/sec at a fetch of 20 cm and 4 cm/sec at 30 cm of fetch.

Figure 9 contains two sets of measurements of wave energy versus fetch with an airspeed of 850 cm/sec. A nearly fixed position identified at the beginning of each wave row is referred to as a "source point." The fetches of the source points and the approximate ends of wave rows are shown. Two different high-pass filters nominally passing frequencies greater than 1 and 10 Hz were used in the rms voltmeter for these experiments. This figure shows drastic changes in wave energy at the locations of the water current changes. The two plots of wave energy versus fetch show very little growth before the source points at a fetch of about 15 cm, rapid growth to a fetch of 25 to 30 cm, and then slower growth as if approaching a saturation.

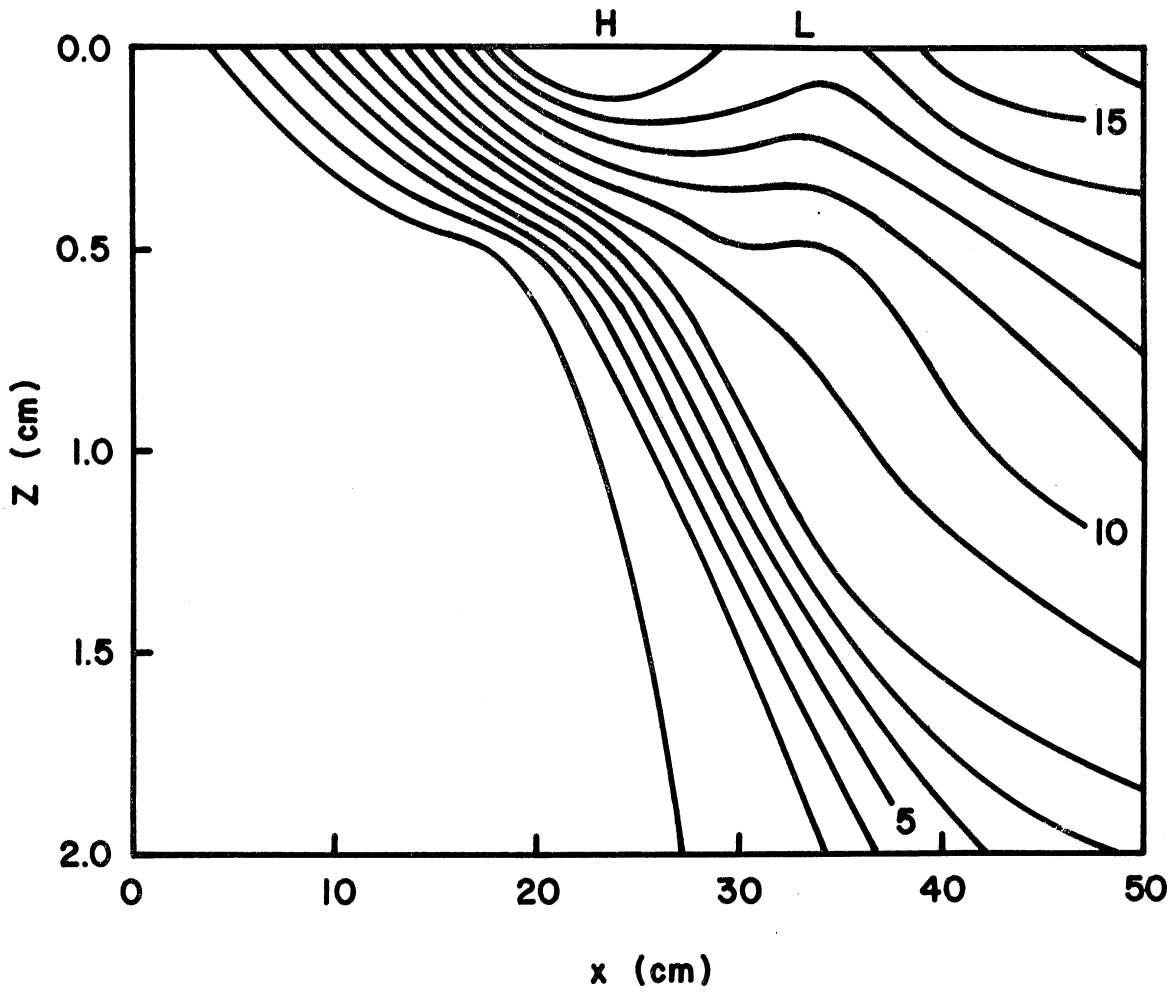

Figure 8. Vertical longitudinal section of water velocity. The contour interval is 1 cm/sec.

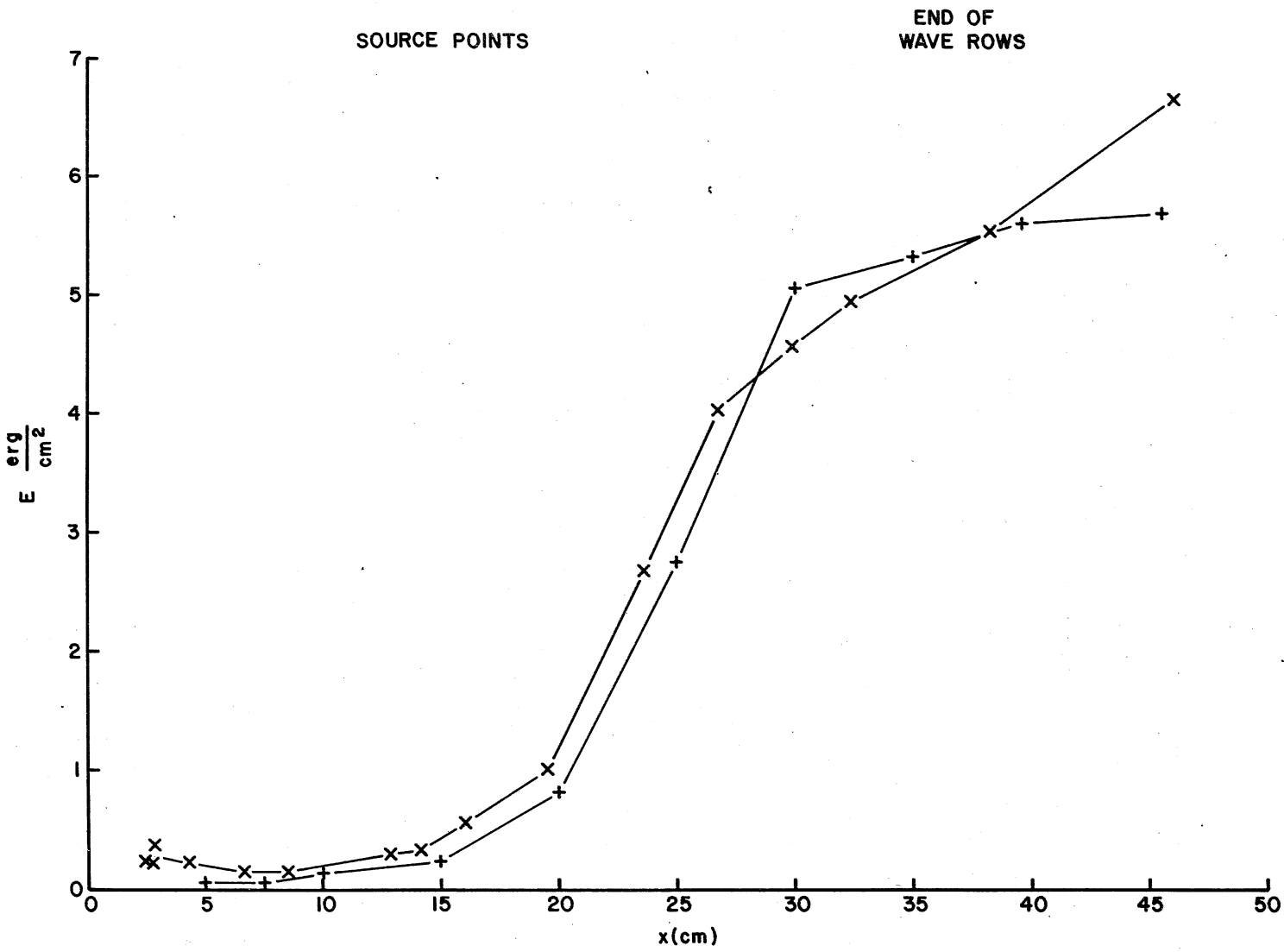

Figure 9. Wave energy versus fetch. The data marked (+) were less filtered than the other.

Wave energy at the same airspeed passed by a sharp high-pass filter with a cutoff at 8 Hz is shown in figure 10. There is a distinct maximum in wave energy at a fetch of 35 cm. The energy at this fetch was nearly as great as the less filtered values in figure 9. After the initial wave development, the filtered high-frequency wave energy was nearly constant to a fetch of at least 400 cm, although the lower frequency waves were seen to be much greater. The capillary-gravity waves grew and approached saturation before lower frequency waves developed significantly.

Figure 11 shows wave energy at a fetch of 400 cm as a function of time as the airflow was increased suddenly. Air leakage over the water surface before opening the blower, and possibly motor vibration, led to very small amplitude waves with a frequency of 2 crests/sec. These apparently did not play a role in the further development of the wave field. Only slight wave growth occurred during the first 15 sec of fast airflow; the waves had a frequency of 15 crests/sec. The rate of wave energy growth next increased abruptly to a peak in energy. Approximately 95 percent of the wave energy at the peak arose during the period of rapid growth. The crest frequency of the rapidly growing waves was only 7 crests/sec. The wave energy then decreased to about 10 percent of the peak. Repeated experiments give somewhat different results, but the pattern of wave growth described here was found repeatedly.

The measurements of wave energy at different fetches in figures 9 and 10 were replotted on a semilogarithmic graph in figure 12. The

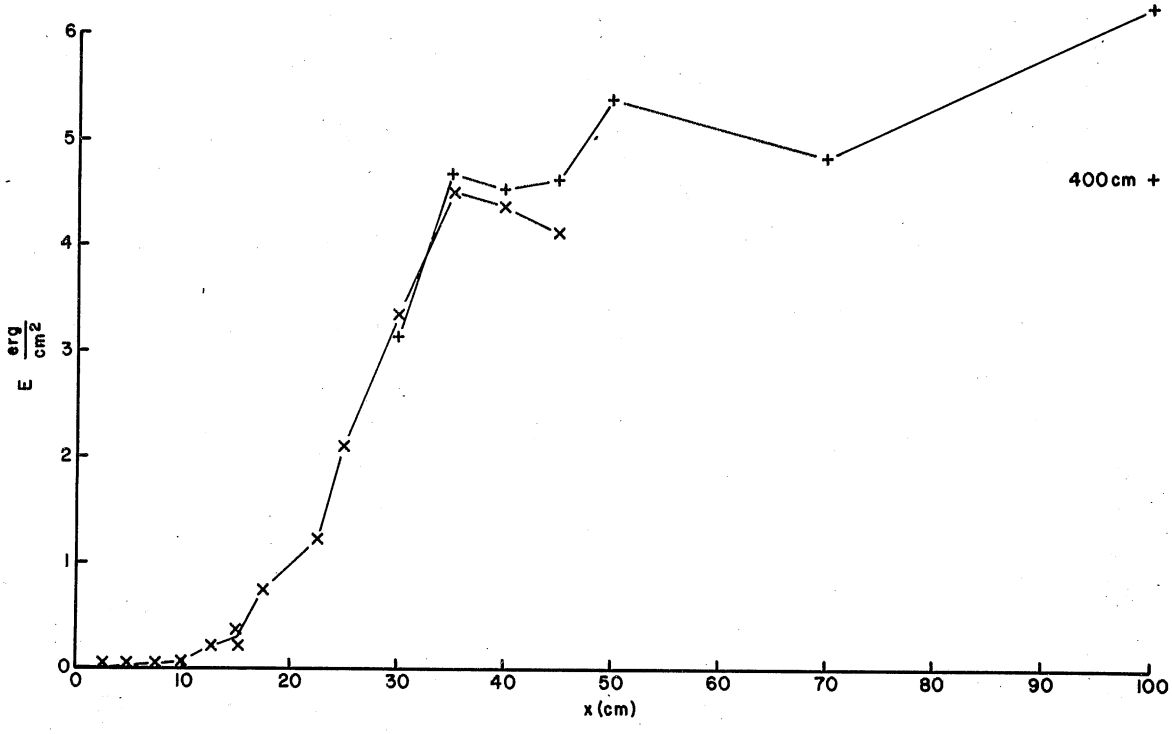

Figure 10. Filtered wave energy versus fetch.

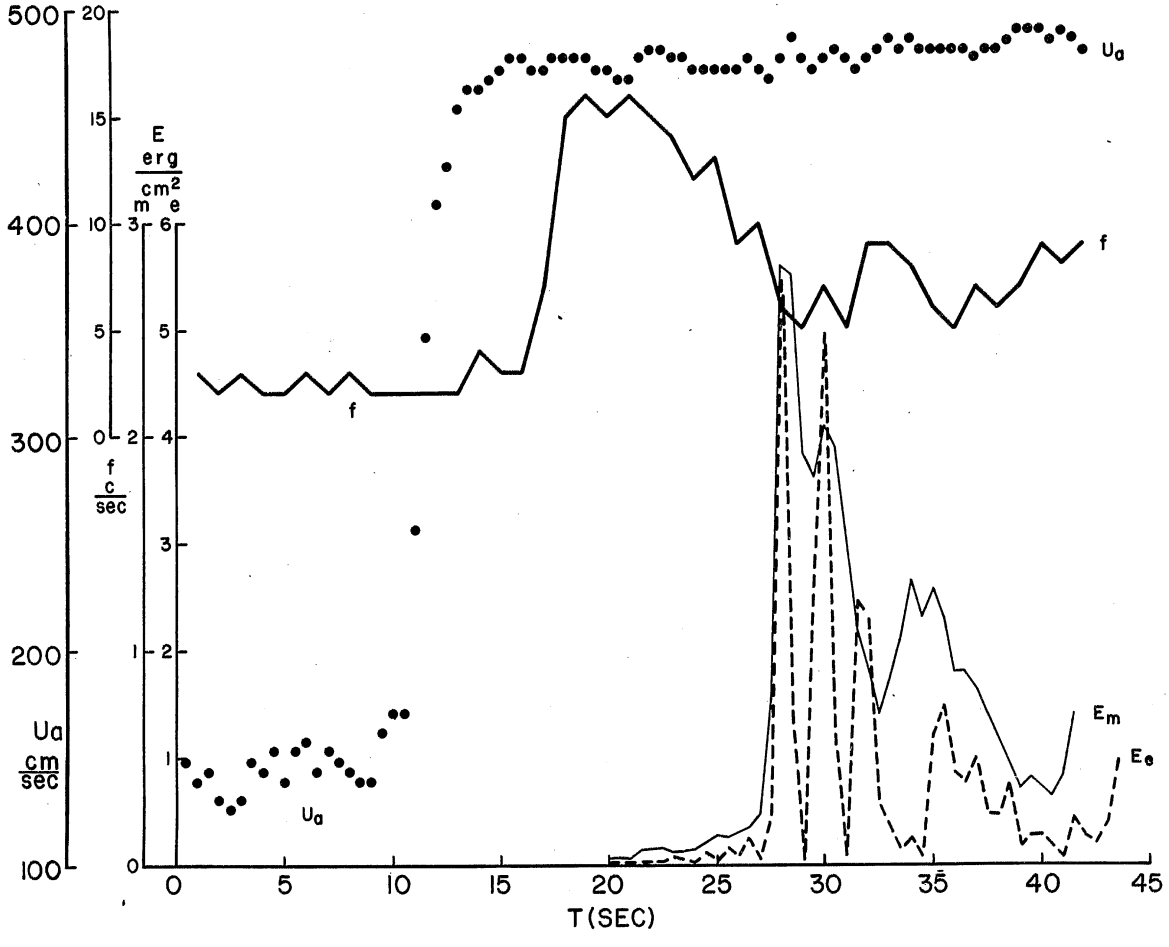

Figure 11. Wave energy versus time after the start of increased airflow. The wave energy was measured with a meter (E_m) and calculated from the width of the wave envelope (E_e). Airspeed (U_a) and crest frequency (f) are also plotted.

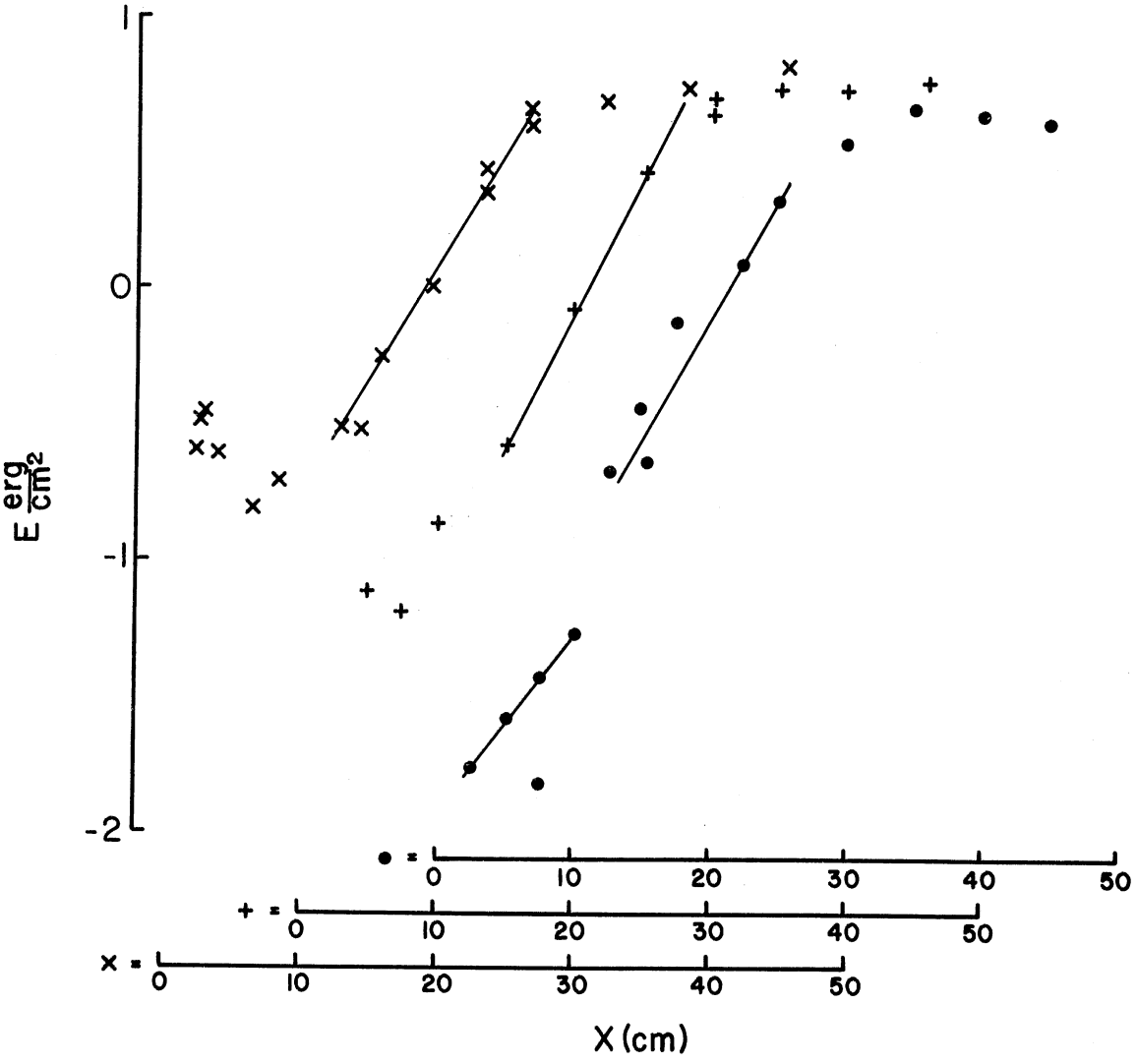

Figure 12. Wave energy versus fetch during three experiments in figures 9 and 10.

measurements of wave energy versus time in figures 11 and 15 were replotted in figure 13. Line segments were drawn to show linear sections of the plots. The very different energy levels in figure 13 are attributed to the different airspeeds. The plot of wave energy versus fetch in figure 12 shows that approximately 90 to 95 percent of the wave growth occurred in an exponential manner between about 15 and 25 to 30 cm of fetch. In the less filtered data, the early wave growth was obscured by unrelated lower frequency waves, but the plot of filtered data shows an earlier exponential growth stage of small amplitude waves. Similarly, the replot of wave energy versus time shown in figure 13 shows two stages of exponential wave growth. The waves in the first, minor stage were found to have a frequency near 15 crests/sec, and those in the major stage had a frequency near 7 crests/sec.

Figure 14 contains hot-film anemometer measurements of water velocities at a depth of 0.2 cm and a fetch of 50 cm as the airflow was started slowly. The normalized square of the width of the velocity fluctuation envelope and the airspeed were also plotted. This figure shows that when the airflow increased gradually, the water velocity increased rapidly; but it decreased abruptly as the steep waves developed. The velocity decrease may be associated with the dips in surface velocity in figures 7 and 8.

A similar experiment with a fetch of 365 cm, a velocity probe depth of 0.3 cm, a wave gage, and a rapidly started airflow is shown in figure 15. The water velocity probe gave erratic readings when the

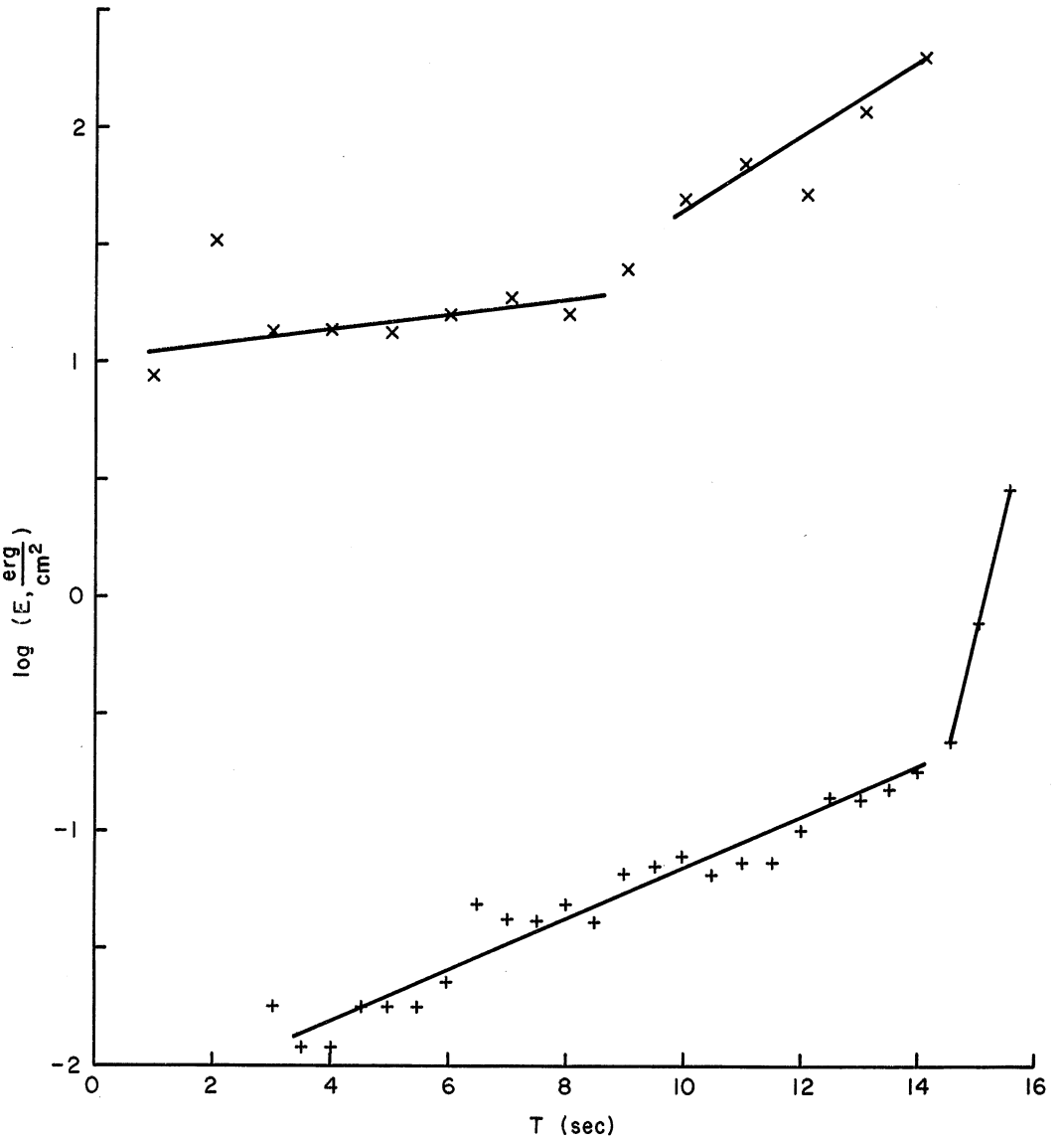

Figure 13. Wave energy versus time. Data are replotted from figures 11 (+) and 15 (x).

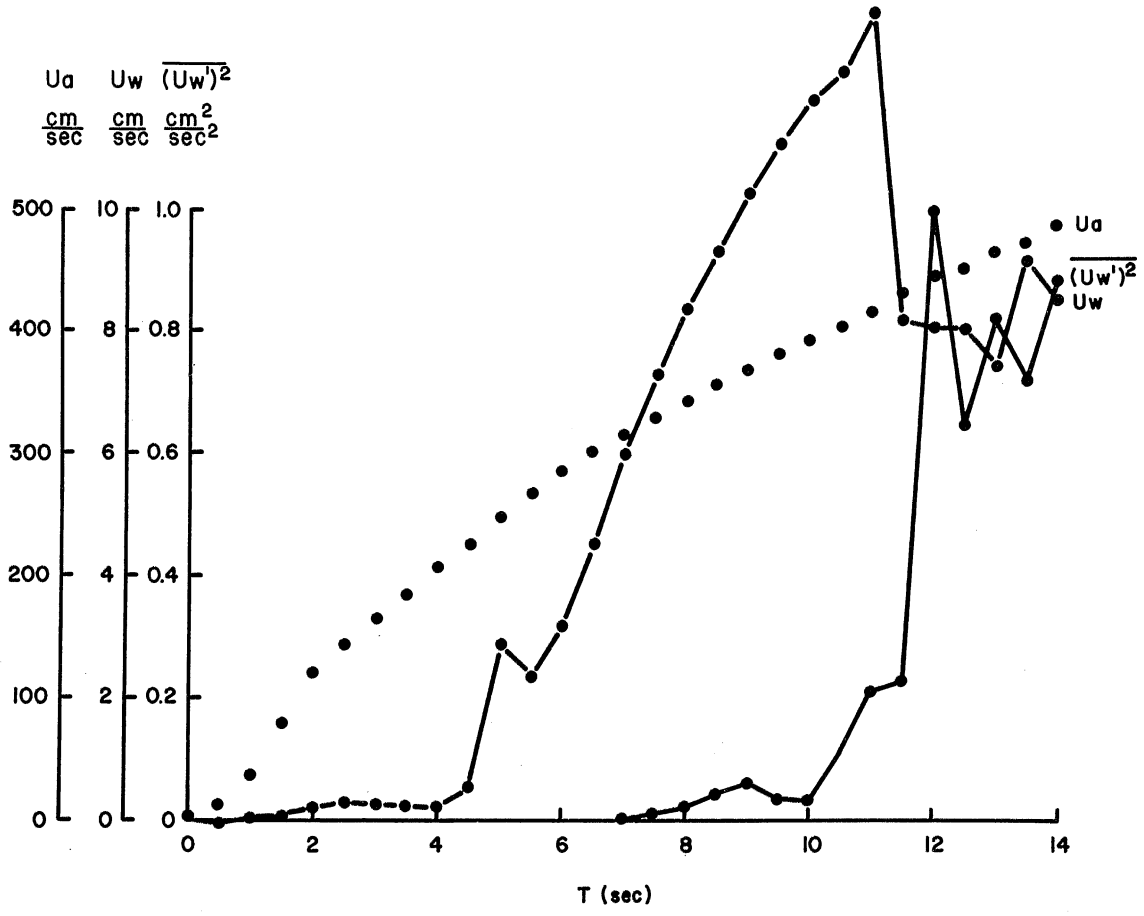

Figure 14. Near-surface water velocity versus time. The short-term average velocity U_w (dashed line), the square of the velocity fluctuations $(U_w')^2$ (continuous line), and the airspeed U_a (dots) are shown.

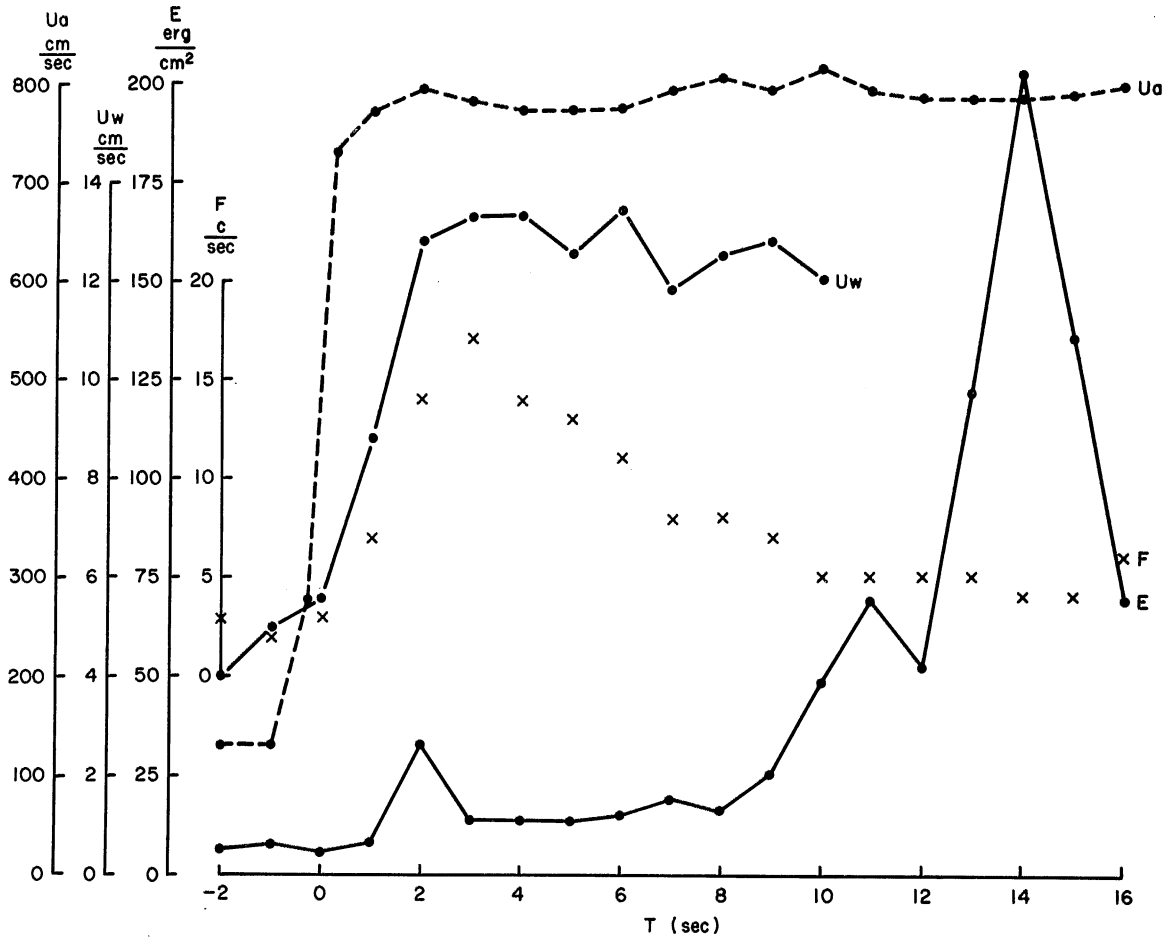

Figure 15. Near-surface water velocity and wave energy versus time. The mean velocity (U_w) is interrupted as the wave energy (E) increases. Airspeed (U_a) and wave crest frequency (F) are included.

waves appeared. Wave energy was calculated from the width of the wave envelope, and the frequency plot represents numbers of wave crests. The near-surface velocity rose rapidly when the fast airflow began, and only later did significant waves appear. In experiments in which the velocity probe was at a depth of 0.5 cm or greater, the increase in velocity was delayed until the steep waves appeared.

In a different but similar wind tunnel installation, an infrared radiation thermometer viewed a 30-cm diameter circular area of the water surface at a fetch of 150 cm and a maximum airspeed of 600 cm/sec. Figure 16 shows the surface temperature changes when the blower was turned on. The water surface temperature changes are consistent with the changes in water circulation described above. The water surface temperature decreased as the airflow developed, rose suddenly as steep waves appeared in the measurement area, and then became steady at an intermediate value. The rise in surface temperature is taken to represent the beginning of vertical mixing indicated in figures 7 and 8.

In addition, the difference between surface and bulk water temperatures was recorded using the infrared radiation thermometer mounted above a water surface at a fetch of 190 cm at different airspeeds. As the airspeed increased, the line of source points moved upstream past the radiometer, and the water surface there became rough. Figure 17 shows a series of measurements over smooth and rough surfaces and a second more detailed series over a rough surface. The variation in surface temperature depression at a single fetch with airspeed further

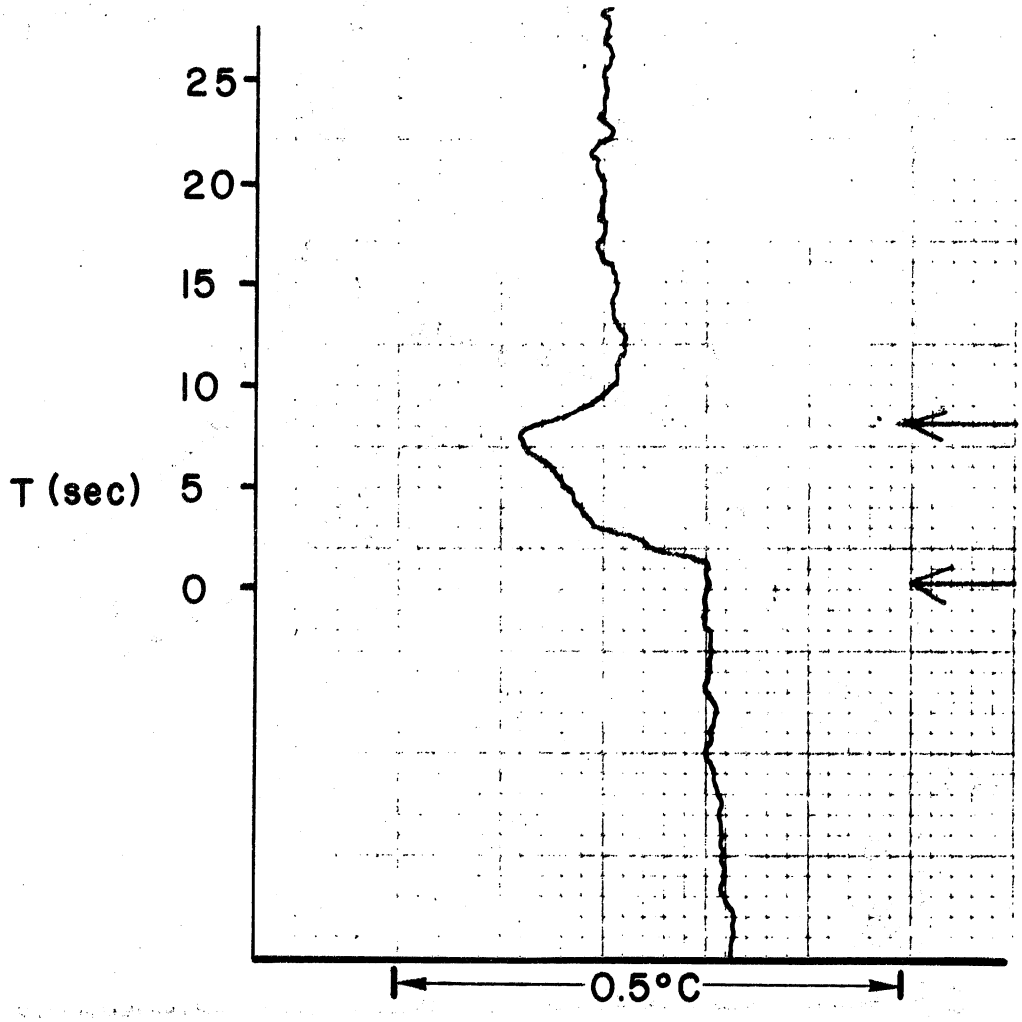

Figure 16. Water surface temperatures versus time after an airflow began. Arrows mark the start of the airflow and also show the time that the water surface beneath the radiometer became rough.

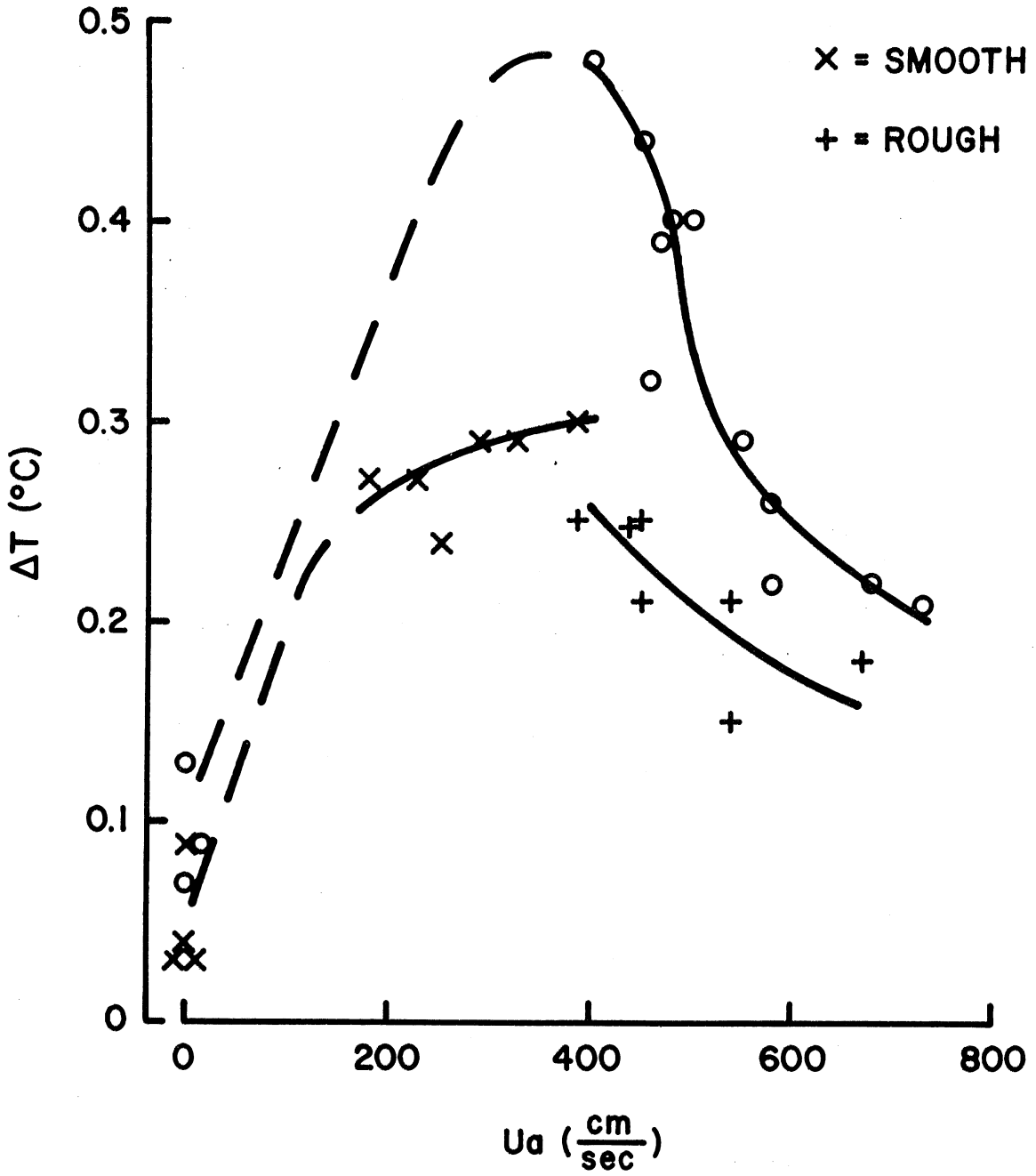

Figure 17. Two series of measurements of water surface temperature depression versus airspeed. In one series, the surface was characterized as either smooth or rough during each measurement.

demonstrates changes in water circulation at the transition. Although there is a gap in the data at low airspeeds, the data show the depression to increase with airspeed where the surface was smooth, the appearance of an apparent discontinuity, and then a lessening of the depression with airspeed above the rough surface. The waveform transition was within the measurement area at the discontinuity in the temperature depression curve. A second, higher set of readings shows the shape of the temperature depression curve downstream of the transition to be concave, opposite to the shape of the curve upstream.

The photograph in figure 18 shows the initial wind waves on a water surface. The width of the scene was about 90 cm. The small-amplitude water waves were regular and long-crested. Rapidly growing waves developed only well downstream, had short-crested "dimple" shapes, and were mostly in rows alined along the direction of the airflow. Irregular larger waves formed downstream of the wave rows.

Figure 19 is a nearly vertical photograph of the water surface where the steep waves first appeared. The regular precursor waves had a wavelength of about 1.8 cm. Dimple-shaped waves developed from the troughs of the precursor waves.

The oblique photograph in figure 20 is a 0.5-sec time exposure of the surface reflection of a floodlamp on the same region of a water surface. The time exposure demonstrates that succeeding dimples formed in the same location, and each followed the previous one to give rows of dimples with bands of smooth water between. The source points of the

Figure 18. Upwind portion of a water surface disturbed by an airflow.

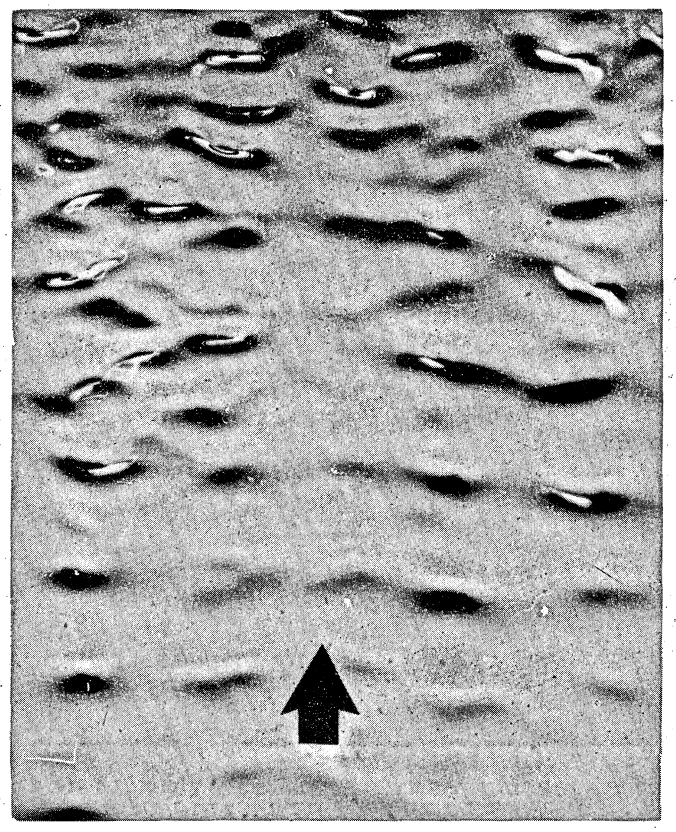

Figure 19. Initial wind waves. The length of the arrow represents 1.8 cm. Bright spots in the dark wave troughs resulted from multiple reflections.

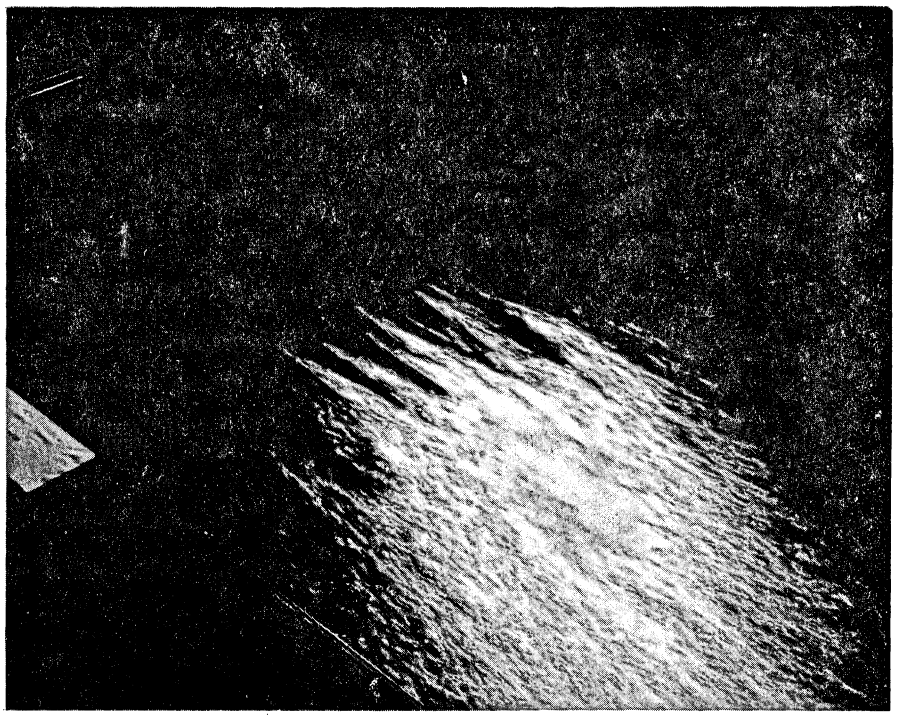

Figure 20. Time exposure of transitional waves in rows. The diameter of the area of reflection was about 50 cm. The light bands in the upwind portion of the reflection were given by steep, short-crested waves moving downwind; the dark bands between them were regions of smooth water.

steep waves remained in one position for several seconds before shifting rather abruptly to a new configuration.

Figure 21 shows the variation in fetch of source points with airspeed as observed by eye. The mean fetch as well as the mean crosswind separation varied approximately as the reciprocal of the square of the airspeed. The fetch was less with more turbulent airflows and also varied with water level. As the level was raised and water overflowed into the entrance duct, the source points moved upstream and passed into the entrance duct when the water depth in the duct was on the order of 0.2 to 0.3 cm. When alternatively a false bottom was installed in the tank to give shallow water depths, the fetch to source points and the initial waves appeared to be affected only at depths of less than 0.3 cm.

A drop of fluorescein dye solution falling a short distance onto the upwind surface of water beneath a slow airflow separated into a patch of surface film and a subsurface blob connected by a thin streak of dye. The surface film drifted downstream and separated into patches on the surface passing between wave rows. The dye streak became stretched downstream between two wave rows and appeared to undergo rotation about a longitudinal axis. When the dye encountered the edge of a compacted surface film, it moved as if the compacted film were a solid boundary. Floating dust particles also showed these surface circulations.

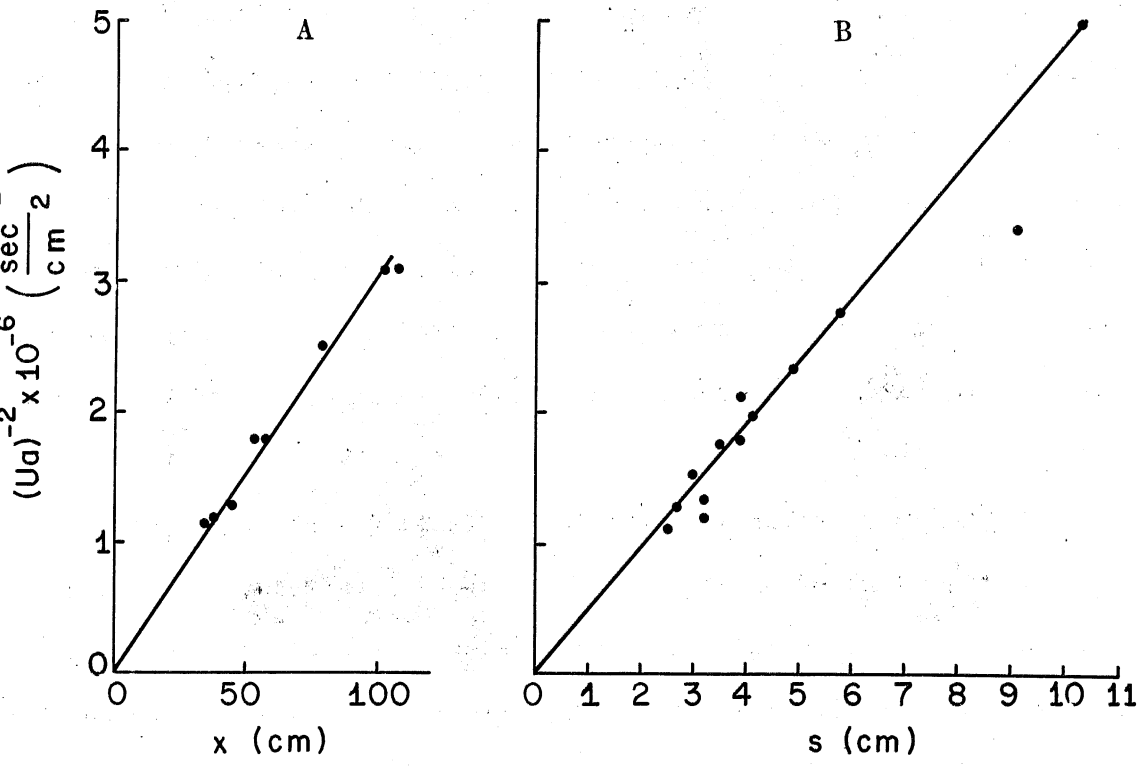

Figure 21. Fetch of source points (a) and traverse spacing (b) versus airspeed.

V. DISCUSSION

The present experiments furnish a description of the intermediate patterns of wave and current flow during the development of wind waves and wind-driven water turbulence. Different stages in the development of waves and current preceded the appearance of the gravity and capillary wave pattern characteristic of wind waves and water turbulence. In most respects, the upstream patterns at different fetches with a steady airflow were duplicated at a fixed fetch downstream when an airflow was started abruptly, and the two situations are combined in a description of the major features of wave and current development.

The first developing waves were regular with long crests. In these experiments, the wave length was near 1.8 cm and the frequency was near 15 Hz, about that of capillary-gravity waves of minimum phase speed. The energy of these precursor waves increased with fetch sometimes to a value near 0.2 to 0.3 ergs/cm, approximately 5 percent of the wave energy after the next growth phase. With a steady airflow, the form of the early wave energy growth was obscured by reflected and other unrelated waves on the surface, but the energy through a high-pass filter increased exponentially. These other waves were absent when the airflow was started abruptly, and the first growth rate was clearly seen to be exponential. A laminar boundary layer with a smooth velocity profile developed in the water.

The transition between the first and second phases of wave development was marked by a transverse line of source points on the water

surface, each of which emitted a rapid series of steep, dimple-shaped waves. Each dimple developed from the trough of a small-amplitude precursor wave. For some distance downstream of the source points, the dimples tended to travel in rows parallel to the direction of the airflow. When the airflow was started abruptly and after several seconds of development of precursor waves, the row of source points appeared at the appropriate fetch in the upwind portion of the water tank. The transition from precursor waves to dimples in rows moved rapidly down the tank, possibly at the airspeed, so that rows of dimples momentarily covered nearly the entire water surface.

The transition region also had an exponential increase in wave energy. The growth factor was more than 10 times greater than previously measured when the airflow was started abruptly, and most of the wave growth occurred during this phase. The wave frequency decreased by about one-half before the waves became highly irregular. The wave amplitudes decreased after this phase and later developed again. With an abruptly increasing airflow, the steep transition waves appeared to be in packets.

The pattern of rows of dimples continued until a wave energy of about 5 erg/cm^2 was attained. The waves then developed, apparently through some intermediate patterns, to long-crested, separate gravity and capillary waves. With further development, the gravity and capillary waves continuously showed greater differences in frequency; the gravity waves increased in amplitude while the capillary waves appeared

to be saturated in energy. The final pattern was characteristic of wind waves on larger, open bodies of water.

In all cases, the waveform transition was accompanied by a transition from a laminar waterflow to turbulence. Particles floating on the surface and dye within the upper water indicated shallow longitudinal water vortexes with surface convergences between the rows of waves. The depth region of significant currents increased from less than 0.5 to more than 2 cm, and the surface speed decreased slightly over a short distance. The water surface temperature reflected this flow change. At successively greater airspeeds, the surface temperature at one position decreased (when the water was being cooled by the air) at a decreasing rate; but the temperature increased with airspeed after the transition, again at a decreasing rate. When the airflow was started abruptly, the water surface began to cool; but at the appearance of steep waves the surface warmed abruptly, and the temperature became constant at an intermediate value.

The velocity profile in the turbulent flow region (fig. 6) shows a linear region near the surface. This is believed to be the first direct demonstration of a viscous sublayer in water at the free surface. The viscous sublayer is significantly thinner at a free surface than at a solid wall. The difference could result in part from the less restrictive boundary condition at the air-water interface.

The relation between the fetch to the wave source points and the airspeed is in accord with a general relation between air stress τ and

transition fetch x_c of current and waves obtained through a dimensional analysis. Several quantities appear in the analysis, but considerations of the mechanisms reduce the number of independent quantities. Stress and viscosity υ are considered to act only upon water currents, with density ρ, as in the combination $\tau/\rho\upsilon$. Surface tension Γ and gravity g act with density only to propagate capillary-gravity waves, and a ratio having dimensions of velocity can be written $(\Gamma g/\rho)^{1/4}$. One form of dimensionless ratio of the pertinent quantities is $\pi = \frac{\tau x_c}{\rho\upsilon(\Gamma g/\rho)^{1/4}}$. Some previous laboratory studies have found stress approximately proportional to the square of the airspeed (e.g., Shemdin, 1972) so that transition fetch may vary as the reciprocal of the square of the airspeed. The relation τx_c = constant implies that the kinetic energy of the flow at transition has a fixed value. The variation of transition fetch with the smoothness of the intersection at the bottom of the air entrance duct and the water surface demonstrated a variation in stress as did the fetch dependence on the turbulence in the air. However, observations that the fetch was not affected by bottom depth at depths greater than a few millimeters illustrate the shallowness of the circulation determining the transition.

Water velocity shear near the surface leads to an interaction between the flow and waves at transition. Some shear persists downstream, and some interaction must continue throughout a rough water surface. The correlation between waves and current may have implications to problems of air-sea interaction. The Miles and Phillips theories of wind-wave generation treat only the influence of air pressure (Kinsman, 1965)

and do not pertain to a waterflow-mediated generation of initial steep waves. Longuet-Higgins (1969) suggested that major waves grow by energy transfer from short waves, but gave no further suggestion of the means of short wave growth. Additional study of the energy transfer from water current to waves appears desirable. Also exchange rates between the sea and atmosphere frequently are limited by the rate of diffusion across the viscous sublayer in the water. The thickness of the layer thus partly controls the exchange rate, and this thickness is less than in corresponding flows at a solid boundary. Further, current theories of laminar-turbulent transition at a solid boundary cannot apply near a free surface.

VI. CONCLUSIONS

The initial growth of steep waves beneath an airflow proceeds by a unique mechanism involving three-dimensional wave shapes and an interaction with the shear flow of the water near the surface. Water turbulence near the surface is modified by the waves and the free motions of the surface. A viscous sublayer exists beneath the water surface, but is thinner than near a solid boundary.

VII. ACKNOWLEDGMENTS

William Everard designed and constructed the special electronic equipment. Figures 16 through 21 were obtained while at the Scripps Institution of Oceanography, La Jolla, Calif.

VIII. REFERENCES

Hires, R. I. (1968), An experimental study of wind-wave interactions, Reference 68-5, Chesapeake Bay Institute, The Johns Hopkins Univ., Baltimore, Md., 169 pp.

Kinsman, B. (1965), Wind Waves: Their Generation and Propagation on the Ocean Surface, Prentice-Hall, Englewood Cliffs, N. J., 676 pp.

Kline, S. J., W. C. Reynolds, F. A. Schraub, and P. W. Runstadler (1967), The structure of turbulent boundary layers, Fig. 9b, J. Fluid Mechanics, 30 (Pt. 4):741-773.

Longuet-Higgins, M. S. (1969), A nonlinear mechanism for the generation of sea waves, Proc. Roy. Soc. A 311:371-389.

McLeish, W., R. A. Berles, W. H. Everard, and G. E. Putland (1971), The SAIL 6-m wind-water tunnel facility, NOAA Tech. Memo. ERL AOML-12, Environmental Research Labs., Miami, Fla., 19 pp.

Mellor, G. L., and H. J. Herring (1969), Two methods of calculating turbulent boundary layer behavior based on numerical solutions of the equations of motion, Fig. 3a, in Proceedings Computation of Turbulent Boundary Layers--1968 AFOSR-IFP Stanford Conference, Vol. 1., eds. S. J. Kline, M. V. Morkovin, G. Sovran, and D. J. Cockrell, Thermosciences Div., Dept. of Mechanical Engineering, Stanford Univ., Palo Alto, Calif., pp. 331-345.

Schraub, F. A., S. J. Kline, J. Henry, P. W. Runstadler, Jr., and A. Littell (1964), Use of hydrogen bubbles for quantitative determination of time dependent velocity fields in low speed water flows, Report MD-10, Div. of Engineering Mechanics, Stanford Univ., Palo Alto, Calif., 66 pp.

Shemdin, O. H. (1972), Wind generated current and phase speed of wind waves, J. Phys. Oceanogr., 2:411-419.